Article

Label-free 3D-CLEM Using Endogenous Tissue Landmarks

Correlative Light and Electron Microscopy

in vivo 2-P

vibratome sections

localization of landmarks

3D-reconstruction

FIB/SEM preparation

re-localization in SEM

FIB/SEM

Manja Luckner, Steffen Burgold, Severin Filser, ..., Eric Hummel, Gerhard Wanner, Jochen Herms

jochen.herms@med.uni-muenchen.de

HIGHLIGHTS

Flat embedding of vibratome sections for precise correlation of LM and SEM

Endogenous landmarks are ideal fiducials for CLEM

The glass slide serves as an absolute reference for precise alignment in yz

Correlation of perisynaptic ensheathment and dendritic spine lifetime

Article

Label-free 3D-CLEM
Using Endogenous Tissue Landmarks

Manja Luckner,[1,2,6] Steffen Burgold,[2,3,4,6,7] Severin Filser,[2,6] Maximilian Scheungrab,[1] Yilmaz Niyaz,[4] Eric Hummel,[4] Gerhard Wanner,[1] and Jochen Herms[1,2,3,5,8,*]

SUMMARY

Emerging 3D correlative light and electron microscopy approaches enable studying neuronal structure-function relations at unprecedented depth and precision. However, established protocols for the correlation of light and electron micrographs rely on the introduction of artificial fiducial markers, such as polymer beads or near-infrared brandings, which might obscure or even damage the structure under investigation. Here, we report a general applicable "flat embedding" preparation, enabling high-precision overlay of light and scanning electron micrographs, using exclusively endogenous landmarks in the brain: blood vessels, nuclei, and myelinated axons. Furthermore, we demonstrate feasibility of the workflow by combining *in vivo* 2-photon microscopy and focused ion beam scanning electron microscopy to dissect the role of astrocytic coverage in the persistence of dendritic spines.

INTRODUCTION

Studying biological key events within complex model systems relies on dynamic and functional imaging at optimum spatial and temporal resolution. Light microscopy (LM) allows visualization of dynamic cellular events in tissues, whereas electron microscopy (EM) remains the only method so far to reveal the complete subcellular architecture at nanometer resolution (Bourne and Harris, 2008). Correlative light and electron microscopy (CLEM) combines the advantages of both imaging modalities, allowing targeting the events of interest in space and time, using LM and subsequently resolving the ultrastructure of the same volume with EM (de Boer et al., 2015; Karreman et al., 2016a; Mironov and Beznoussenko, 2009). In particular, CLEM has greatly advanced our understanding of complex neuronal connectivity matrices by revealing the ultrastructural architecture and dynamics of neurites and synapses (Blazquez-Llorca et al., 2015; Genoud et al., 2006; Maco et al., 2013, 2014). However, a major methodological hurdle remains the correlation of LM and EM datasets by accurately tracking the position of the region of interest (ROI) within the EM specimen. For voluminous specimens such as the mouse brain, ROIs can be retrieved by screening serial thick (50–100 μm) vibratome sections of the tissue (Li et al., 2011). Nevertheless, serial EM imaging of large tissue samples is very cumbersome and results in unnecessarily large datasets. Currently, LM inspection to confine an ROI within the EM specimen is the most common approach for CLEM. For this purpose, fiducials are needed, which are detectable in both LM and EM. The ROIs can be marked by photo-oxidation of fluorophores (Grabenbauer et al., 2005), by affinity labeling with peroxidases (Knott et al., 2009) or by the use of exogenous fiducial markers like polymer beads (Kukulski et al., 2012), quantum dots (Masich et al., 2006), or near-infrared branding (NIRB) (Bishop et al., 2011). Although useful, these approaches require processing of the tissue samples and thereby might obscure the target structure or even deteriorate their ultrastructure. Alternatively, endogenous landmarks, which surround the ROI providing both LM and EM contrast, can be used as a guide to retrace the position of the ROI following EM processing (Karreman et al., 2016b). Unfortunately, resin embedding for EM preparations covers endogenous landmarks, thus prohibiting marker identification by EM. Although there are some protocols to reduce resin embedding, these methods comprise several delicate preparation steps or specialized equipment (Kizilyaprak et al., 2014; Belu et al., 2016; Lucas et al., 2017; Schieber et al., 2017). These issues were addressed by developing a "flat embedding" preparation to enable direct LM visualization of endogenous fiducial markers, present throughout the brain parenchyma. We show that blood vessels, nuclei, and myelinated axons can be used for precise correlation of LM and EM images with micrometer accuracy, allowing retrieval of structures as small as single synapses. A wide range of optical microscopic modalities, including wide-field, differential interference contrast (DIC), and confocal and reflectance microscopies can be used to visualize these endogenous landmarks with minimal labeling effort or even in a completely label-free manner. The feasibility of the protocol was confirmed by revealing the intimate interplay of perisynaptic astrocytic

[1]Department of Biology I, Biocenter Ludwig-Maximilians-University Munich, Planegg-Martinsried 82152, Germany

[2]German Center for Neurodegenerative Diseases (DZNE), Translational Brain Research, Munich 81377, Germany

[3]Center for Neuropathology, Ludwig-Maximilians-University Munich, Munich 81377, Germany

[4]Carl Zeiss Microscopy, Oberkochen 73447, Germany

[5]Munich Cluster of Systems Neurology (SyNergy), Munich 81377, Germany

[6]These authors contributed equally

[7]Present address: Carl Zeiss Microscopy, Oberkochen 73447, Germany

[8]Lead Contact

*Correspondence: jochen.herms@med.uni-muenchen.de

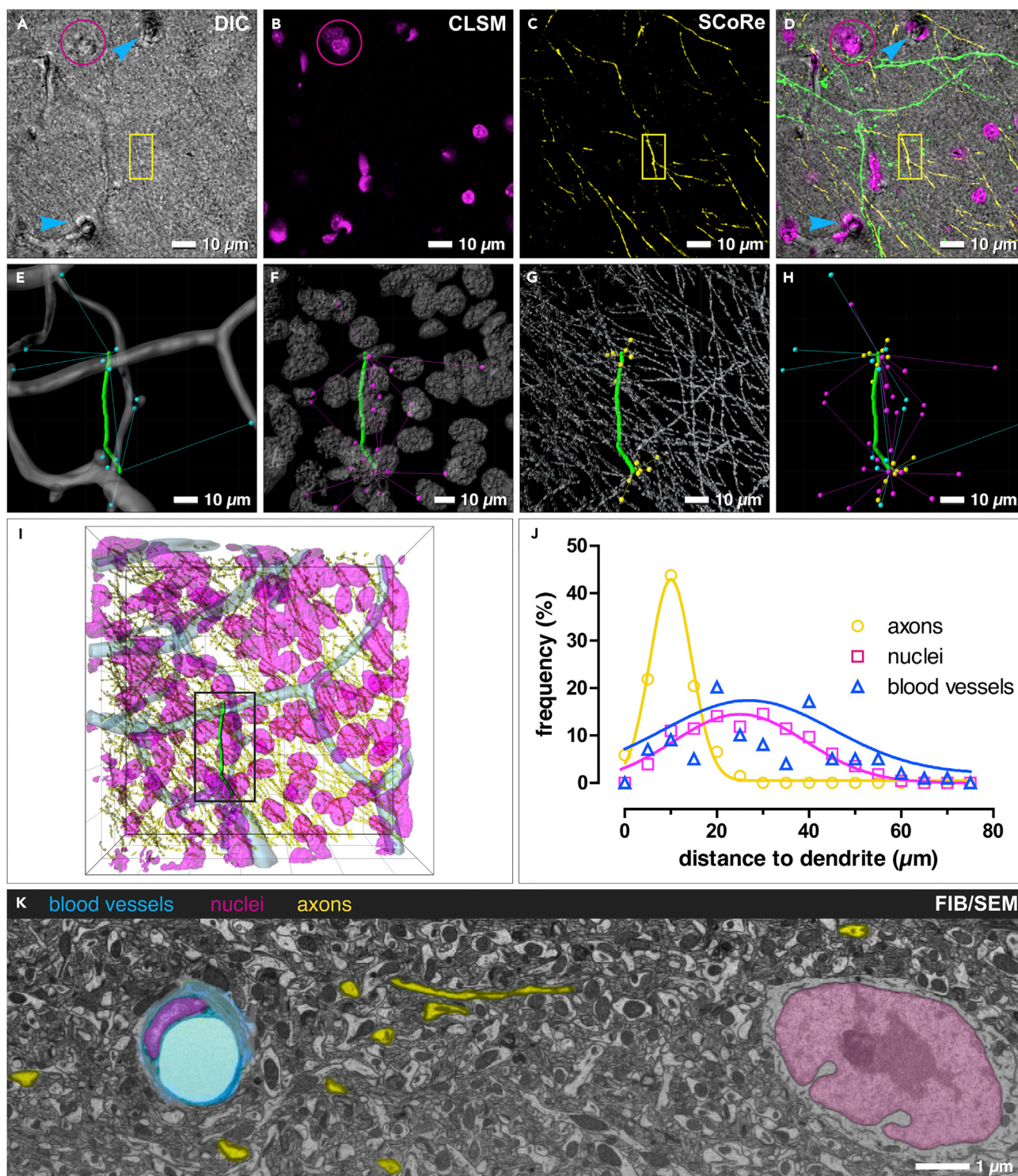https://doi.org/10.1016/j.isci.2018.07.012

Figure 1. Availability and Precision of Endogenous CLEM Landmarks

(A–C) Blood vessels (arrowheads), nuclei (magenta) and myelinated axons (yellow; boxed area) can be visualized by DIC (A), CLSM (B) and SCoRe (C) microscopy.

(D) Overlay of DIC, CLSM, and SCoRe images. Blood vessels (arrowheads); nuclei (magenta); myelinated axons (yellow; boxed area).

(E–H) 3D reconstructions of blood vessels (E), nuclei (F), and myelinated axons (G) with distance traces between target dendrite and closest landmarks (H).

(I) Overlay of the 3D reconstructions of landmarks and the target dendrite.

Figure 1. *Continued*
(J) Frequency distribution of correlative landmarks, plotted against their respective distance to the target dendrite.
(K) FIB/SEM micrograph of cortical mouse brain tissue clearly represents blood vessels (blue), nuclei (magenta), and myelinated axons (yellow) by their typical shape and contrast.
Related to Figures S1–S3.

processes and dendritic spines, previously imaged by *in vivo* two-photon microscopy and subsequently relocated and imaged by focused ion beam scanning electron microscopy (FIB/SEM) with nanometer resolution.

RESULTS

Natural Landmarks for 3D-CLEM

Blood vessels, nuclei, and myelinated axons are excellent fiducial markers for 3D-CLEM since they fulfill the following criteria: (1) sufficient contrast in LM and EM, (2) distinctive size and shape, and (3) sufficient density to restrict the volume of correlation (Figure 1). They can be readily recognized by DIC (Figure 1A) and FIB/SEM (Figure 1K). The precise 3D position of these landmarks in proximity to the target dendrite can be mapped by various confocal microscopic techniques (Figures 1A–1C). Confocal laser scanning microscopy (CLSM) enables high-resolution imaging of nuclei, stained with the cell-permeant DNA-binding dye DRAQ5 (Figure 1B). Since DRAQ5 is a vital dye, tissue permeabilization can be omitted, which bears the risk of ultrastructural deterioration. In addition, spectral confocal reflectance microscopy (SCoRe) (Schain et al., 2014) can be used for direct, label-free visualization of myelinated axons (Figure 1C). Spatial distances between a randomly selected dendritic segment and its surrounding landmarks in cortical layer I were determined to confirm that landmarks are sufficient for precise CLEM alignment (Figures 1E–1J). The average distance between a dendrite and either blood vessels (Figure 1E) or nuclei (Figure 1F) equaled 25.5 μm or 26.7 μm, respectively (Figure 1J). The distinct morphology of both markers facilitated the identification of ROIs by triangulation of the landmarks. Myelinated axons (Figures 1C and 1G) are present in higher density and subsequently at closer vicinity to the target dendrite, with an average distance of 9 μm (Figure 1J), thus further increasing the precision of ROI retrieval.

"Flat-Embedding" Preparation for CLEM

To demonstrate the applicability and precision of the presented CLEM preparation method, several ROIs with Thy1.2-eGFP-expressing dendritic tufts in the somatosensory cortex of Thy1.2-GFP-M mice (Figures 2A–2C) were imaged by *in vivo* 2-photon microscopy and subsequently relocated in vibratome sections (Figures 2D–2F). Vibratome sections were immobilized on glass slides to maintain specimen orientation during LM and EM preparation. To identify the sections containing the ROI, brain slices were recorded with an epifluorescence microscope to reconstruct the dissected cortex with an imaging software (Adobe Photoshop), based on its unique blood vessel pattern (Figure 2D).

ROI-containing brain sections were further processed for EM (Figure 3A). Excessive resin, covering the brain tissue, was removed by draining and centrifugation to enable direct macroscopic inspection of the tissue surface (Figures 3B and 3C). Superimposition of bright field (Figure 3B) and SEM (Figure 3C) micrographs, based on the characteristic outline of the brain section, was sufficient for an immediate macroscopic correlation. The preparation protocol preserved the integrity of the specimens without major tissue shrinkage or corrugations (Figures 3B and 3C), as could be expected from dehydration. Suitable fiducials for CLEM could be identified in SEM due to the carbon coating of the specimen: since carbon has lower yields of backscattered electrons (BSE) and secondary electrons (SEs), compared with heavy metals, it appears transparent and superficial structures of the tissue become detectable. Structures lying in greater depth become visible by slightly increasing the accelerating voltage (Figure S1). The distinctive sizes and shapes of the apparent natural landmarks (blood vessels appear as channels or large holes, nuclei as dark dots) were used for the subsequent superimposition of light and electron micrographs, to define the target area in x/y direction (Figures 3D–3F).

3D Landmark Correlation of LM and FIB-SEM Datasets

After identification of the target area on the specimen surface, FIB milling was used to gain access into the brain tissue containing the dendrite of interest, which was previously imaged by *in vivo* 2-photon microscopy. Milling time, and consequently costs, were reduced by milling the trench toward the volume of interest with high beam current, which was stepwise decreased, while approaching the final block face of
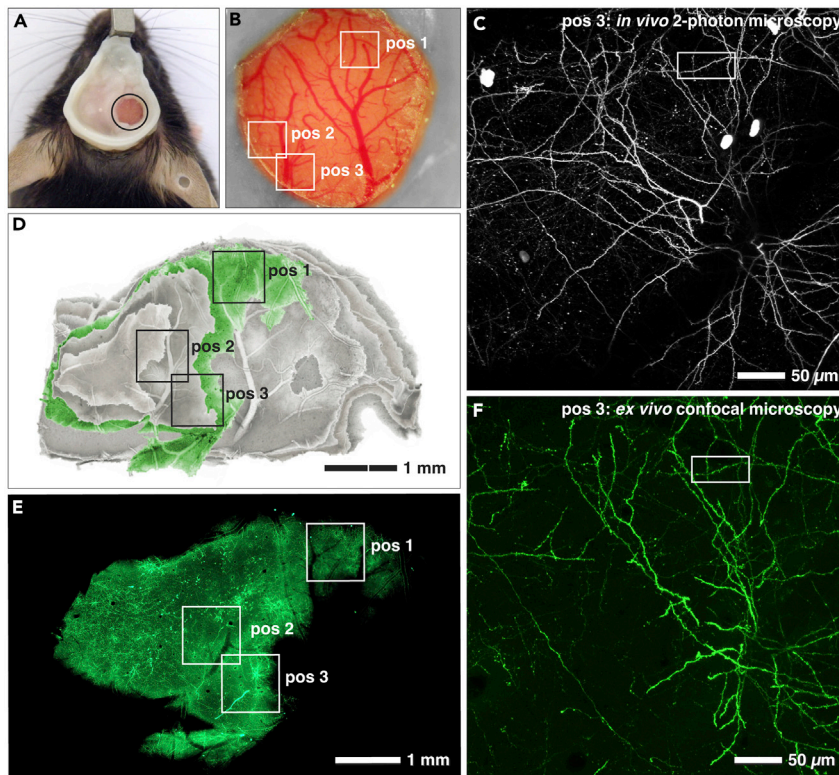
Figure 2. *In vivo* and *Ex Vivo* Light Microscopy for CLEM

(A) Cranial window implantation gives optical access to the cortex of the mouse brain.

(B) Magnified image section of cranial window in (A). The blood vessel pattern enables the retrieval of previously imaged positions (framed areas: pos 1–pos 3).

(C) Maximum intensity projection of *in vivo* 2-photon image stack of pos 3 (framed in B). Framed area designates the target dendrite at the last imaging time point (day 41).

(D and E) Reconstruction of the cortex by alignment of vibratome sections (D), based on the blood vessel pattern, facilitates identification of the brain slice (green) containing the target dendrites of three different positions (pos 1– pos 3) (E).

(F) Maximum intensity projection of *ex vivo* CLSM image stack of pos 3 (D and E). Framed area designates the target dendrite [compare (F) with (C)].

70 × 50 μm (Figures 4A–4C). Since block-face micrographs exhibit sufficient landmarks for correlation, the position of the ROI could be identified by correlating the FIB/SEM 3D reconstructions of nuclei and blood vessels with the corresponding CLSM 3D data in Amira (Figure 4D). A rough 3D reconstruction of the dense axonal network further facilitated the identification of the target dendrite (Figures 3E and 3F; Video S1), thus reducing the ROI to 15 × 15 μm (Figure 4C). The final ROI images were acquired with high resolution (pixel size in x/y: 5 nm) every 15 nm, whereas low-resolution overview images (pixel size in x/y: 27 nm) of the entire block-face area were recorded every 1 μm in z (Figures 4B and 4C) to confirm or eventually adjust the position of the ROI "on the fly."

CLEM of Dendritic Spine Lifetime and Astrocytic Synapse Coverage

The concept of the "tripartite synapse" refers to the functional integration and physical proximity of astrocytic processes with pre- and postsynaptic elements of the chemical synapse (Araque et al., 1999). However, experimental dissection of the morpho-functional relationship between these structures is hampered by the very small size of perisynaptic astrocytic processes (PAPs), which is below the resolution limit of conventional LM (Heller and Rusakov, 2015; Panatier et al., 2014). CLEM in combination with the "flat-embedding" protocol is suitable to study the morpho-functional interactions between PAPs and their corresponding synapses at an ultrastructural level. Hereby, we were able to investigate whether the extent of synaptic PAP coverage correlates with the lifetime of post-synaptic partners. To assess the lifetime of
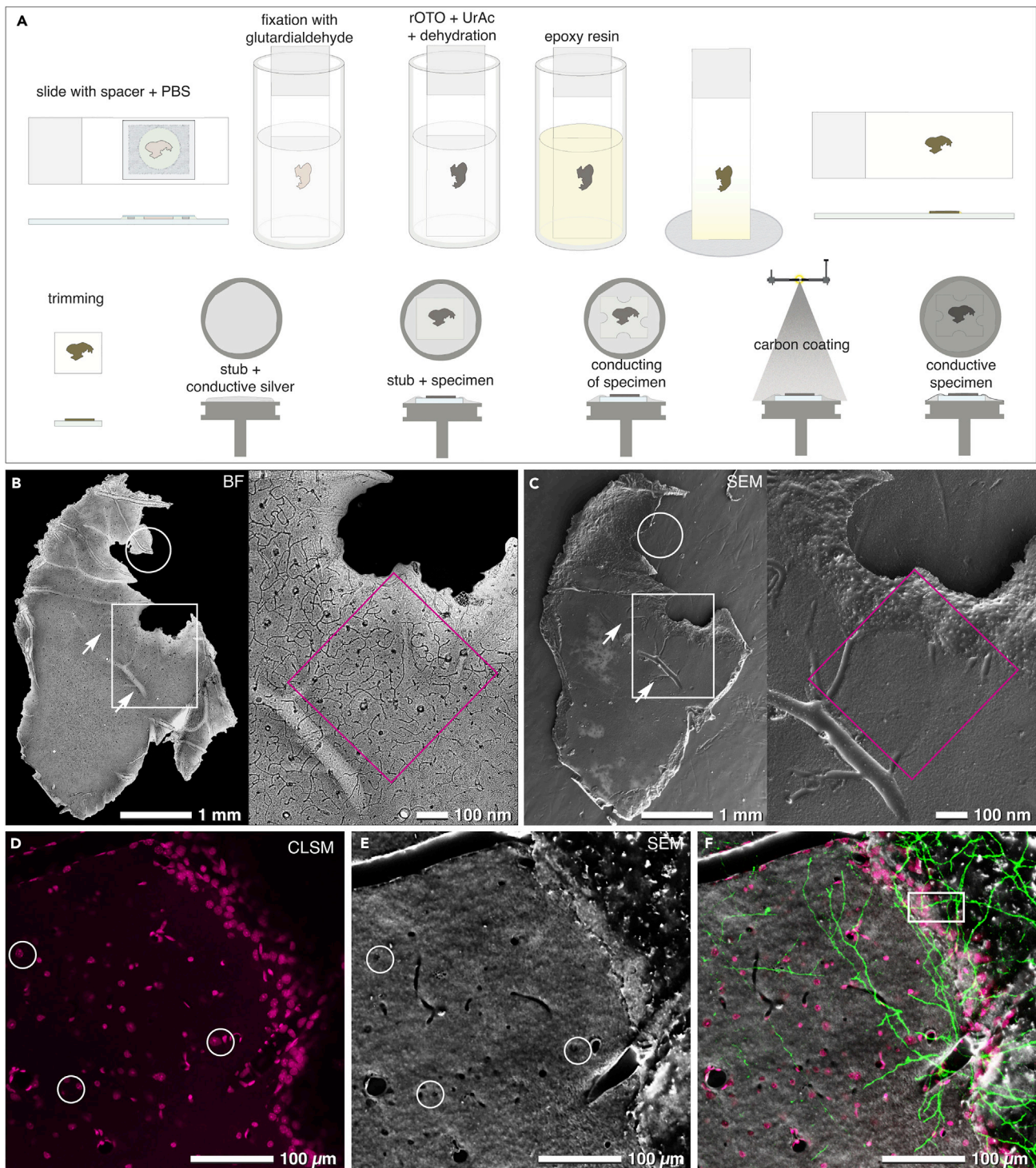
Figure 3. Sample Preparation and Retrieval of Landmarks

(A) Vibratome sections are mounted onto a glass slide with a spacer and sealed by a coverslip. After LM, the coverslip and the spacer are removed. Post-fixation (glutardialdehyde, reduced osmium-ferrocyanide-thiocarbohydrazide-osmium (rOTO), uranyl acetate [UrAC]), dehydration and infiltration with epoxy resin are performed in vials. After removal of excess resin and polymerization, the slide is trimmed to appropriate size. The specimen is mounted with colloidal silver onto an aluminum stub, conducted with bridges of colloidal silver, and coated with carbon (15–20 nm) by evaporation.

(B and C) Comparison of a bright field (BF) micrograph (B) with a scanning electron micrograph (C) of the selected vibratome slice (Figures 2 D and 2E). At low magnification, changes in morphology are easily recognized (B, C, circles). Intersected blood vessels are visible in both images (arrows), serving as the most prominent landmarks.

dendritic spines, chronic *in vivo* 2-photon microscopy in the somatosensory cortex of adult Thy1.2-GFP-M mice (Feng et al., 2000) was performed. The dynamics of eGFP-labeled spines on apical dendritic tufts of layer V pyramidal neurons were monitored before and during enriched environment exposure of mice (Jung and Herms, 2014). As documented by the micrograph time series (Figure 5A), enriched environment substantially and persistently promoted spinogenesis and thus increased the amount of newly formed spines accessible for lifetime analysis. Subsequently, target dendrites were relocated in vibratome sections and respective EM specimen by flat embedding and triangulation of natural landmarks. Correlation of *in vivo* 2-photon microscopy, *ex vivo* CLSM, and FIB/SEM 3D datasets (Figures 5A–5D) demonstrates that structural integrity of the corresponding dendrites and dendritic spines (Figures 2C–2F) was well preserved throughout CLEM preparation. Based on the FIB/SEM tomograms, tripartite synapses were reconstructed in 3D to determine the perimeter of the synaptic cleft and its astrocytic coverage (Figure 5E and Videos S2 and S3). Correlation of these structural parameters with dendritic spine lifetime revealed that the fraction of synaptic perimeter surrounded by PAPs on average amounts to 37% and scales neither with synaptic cleft area nor with spine age (Figures S4A and S4B). The synaptic perimeter of a few old spines (lifetime ≥ 41 days) was even completely devoid of PAPs.

DISCUSSION

Methodological hurdles in CLEM are the re-localization of a rather small target volume within a large tissue volume, changing sample orientation during the transition between different microscopy modalities, and structural distortions or preparation artifacts caused by artificial fiducials (de Boer et al., 2015; Grabenbauer, 2012; Karreman et al., 2016a). Current CLEM approaches, based on artificial fiducials, suffer from several drawbacks (Table 1): (1) labeling with electron-dense precipitate or fluorescent beads/quantum dots can obscure ultrastructural details; (2) fixation and harsh permeabilization conditions, required for antibody labeling, compromise ultrastructure; (3) delivery of tracers to living tissue may induce toxic side effect; and (4) NIRB is mainly used to mark the surface of the sample, as light scattering within the tissue limits the depth of NIRB (Karreman et al., 2014).

To circumvent these technical drawbacks we introduce a "flat-embedding" protocol of vibratome sections, ideal for both SEM and FIB/SEM investigations (Figures 1, 2, S1, S2, and S3). Due to their thickness of approximately 50 μm, vibratome sections can be: (1) adequately fixed, even as large slices (e.g., 20 mm^2), (2) investigated entirely at low and high magnifications with LM and SEM (Figures 3B and 3C), and (3) milled by FIB/SEM in their entire thickness (Figure 4C). Since tissue sections can be permanently immobilized on glass slides, their orientation does not change in the transition from LM to FIB/SEM (Figures 3B and 3C). The complex correlation of LM and SEM data can be achieved by a simple overlay of the LM image, depicting the sample surface, onto the SEM image of the resin-embedded section (Figure 3F), with its characteristic topography (SE image) and material contrast information (BSE image). In addition to the direct surface topography, subsurface information can be gathered at high voltages, as the BSE signal can be detected within a depth of approximately 3 μm at 25 kV (Figures S2 and S3). Thereby, the surface of the specimen becomes transparent and prominent structural features as nuclei and axons become visible with strong contrast (Figure S3). DIC microscopy yields sufficient resolution and depth of field to visualize blood vessels, nuclei, and myelinated axons simultaneously (Figure 1A). Furthermore, SCoRe microscopy can be applied to visualize myelinated axons based on their high refractive index in a label-free manner (Schain et al., 2014) (Figure 1C). Axons are excellent high-resolution fiducials for brain tissue, due to their high density and strong BSE signal in SEM (Figures 1K and S2). As nuclei and blood vessels are abundantly present in all animal tissues, this method can also be used for various organs like kidney, liver, and skin.

A reduction of the laborious FIB/SEM trench milling could be achieved by stepwise adjusting the ion beam current depending on the trench position, thus saving time and costs (Figures 4A and 4B). Monitoring the constantly increasing block face every 0.5–1 μm provides essential information about the position of the relevant landmarks, which can be reconstructed in 3D and compared with the LM stacks for possible corrections or fine adjustments (Figures 4C and 4D). Since the cross-section of the glass slide serves as
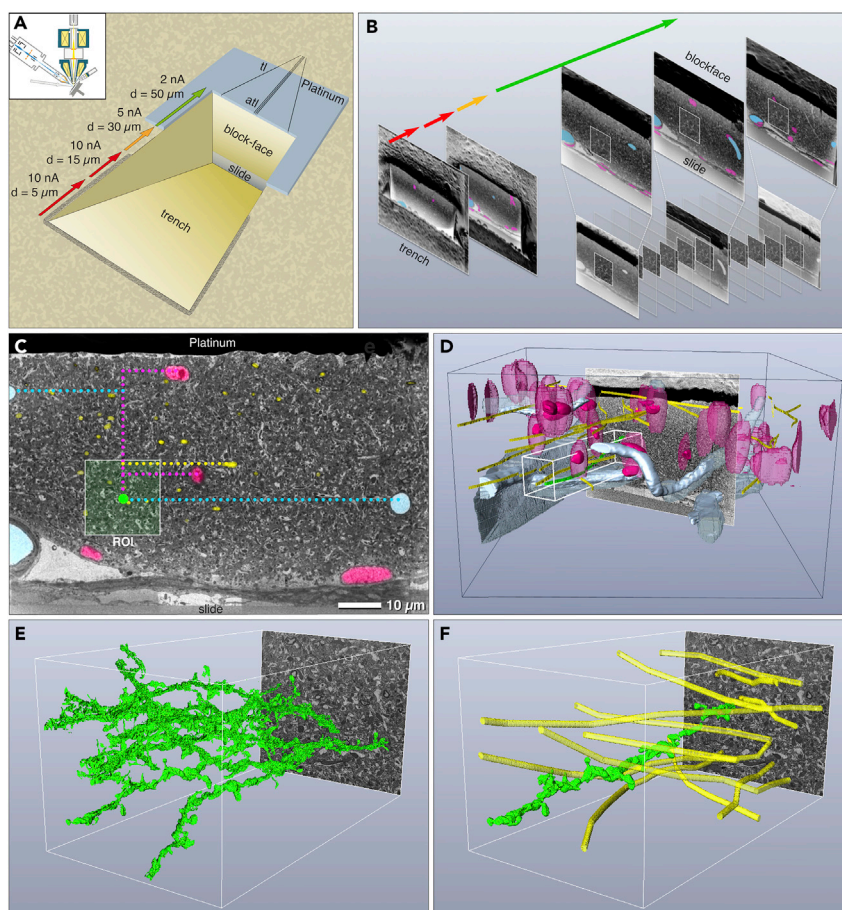
Figure 4. 3D alignment of LM and FIB/SEM Tomograms

(A) Economic trench milling in several steps: successive decrease in ion beam energy with increasing milling depth. FIB/SEM tomography is performed by eucentric tilting of the specimen to 54° into the coincidence point (inset). The target area is coated with approximately 1 μm platinum by ion beam deposition. Thin tracking lines (tl) and autotune lines (atl) serve for controlling the milling/imaging process (section thickness, focus, astigmatism).

(B) High-resolution images (white squares) are taken every 15 nm of milling. In addition, key frames are taken in intervals of 1 μm in z-direction, providing micrographs for fast, "on the fly" 3D correlation of natural landmarks: blood vessels (blue), nuclei (magenta), and myelinated axons (yellow).

(C) When reaching the final block face the region of interest (ROI; white square) with the target dendrite (green spot) is defined in x/y using the coordinates of the landmarks derived from the 3D LM data. Blood vessels (blue); nuclei (magenta); myelinated axons (yellow).

(D) Superimposition of landmarks (blood vessels, nuclei, and axons; transparent) of the LM reconstructions (black box) with the FIB/SEM reconstructions of the corresponding structures (solid).

(E) Preliminary fast reconstructions of several potential dendrites (green) in the target volume (white box) by an automatic labeling algorithm (*Magic Wand*, Amira™).

(F) Usage of myelinated axons (yellow) as correlative marker to identify the target dendrite (green).

Related to Video S1.

absolute reference for precise alignment, an exact correlation is ensured (Figure 4C) (Luckner and Wanner, 2018). These improvements reduce the CLEM workflow and make artificial fiducials and delicate trimming needless (Kolotuev et al., 2012).

The high precision of the presented CLEM method was demonstrated by *in vivo* 2-photon microscopy of single dendritic spines and their subsequent identification within a resin-embedded tissue by FIB/SEM Detailed information could be gathered about dendritic spine lifetime and morphometric measurements of the corresponding tripartite synapse at nanometer resolution (Figure 5). Our data show that astrocytic coverage of the synaptic cleft does not proportionally scale with either the synapse size or the synapse
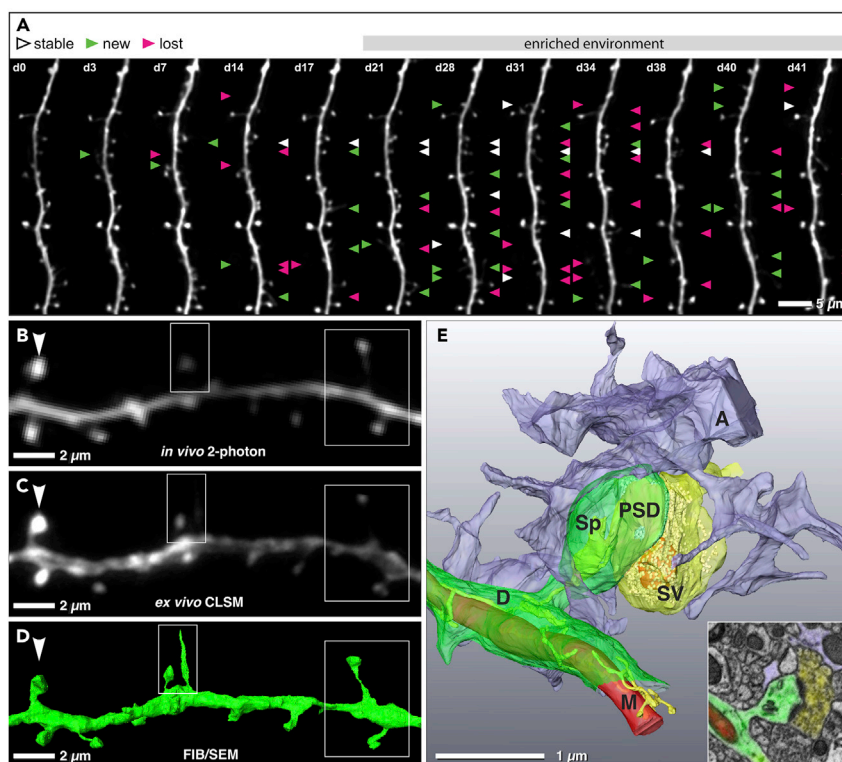
Figure 5. 3D-CLEM of Cortical Tripartite Synapses

(A) *In vivo* 2-photon micrographs of eGFP-labeled apical dendrites of layer V pyramidal neurons in the somatosensory cortex imaged before and during enriched environment. Enriched environment exposure started at day 18 and was continued until end of the imaging period. White arrowheads mark spines that formed newly and remained stable for at least two consecutive imaging time points; gained and lost spines are labeled with green and magenta arrowheads, respectively. Scale bar = 5 μm.

(B–D) Comparative juxtaposition of the same dendritic segment recorded by *in vivo* 2-photon (B), *ex vivo* CLSM (C) and FIB/SEM microscopy (D). White boxes indicate dendritic spines that were detected in high-resolution CLSM microscopy and FIB/SEM; white arrowheads indicate spines that were detected in all imaging modalities. Scale bar = 2 μm.

(E) 3D reconstructed FIB/SEM tomogram of a complete tripartite synapse (A, astrocyte; D, dendrite; M, mitochondrion; PSD, postsynaptic density; Sp, spine; SV, synaptic vesicles). Inset shows a single micrograph of the corresponding FIBS/SEM stack depicting a dendritic spine (green) with associated presynapse (yellow) and astrocyte (purple).

Scale bar = 1 μm.

Related to Figure S4.

age (Witcher et al., 2007), indicating that smaller, newly formed spines, as well as established larger spines, have equal access to extracellular glutamate, which is restricted by astroglial ensheathment of the synaptic perimeter. Thus, astrocytes may facilitate integration of synapses by preventing transmitter spillover between neighboring excitatory synapses (Ostroff et al., 2014). Although we did not detect a change of astrocytic coverage during synapse maturation under basal conditions, it has been shown to increase during periods of enhanced neuronal activity to augment glutamate clearance and preserve synaptic response (Genoud et al., 2006). Furthermore, the observation that the synaptic perimeters of some persistent spines are completely devoid of astroglial processes indicates that permanent astrocytic coverage might not be mandatory for the maintenance of excitatory synapse stability (Bernardinelli et al., 2014) (Figure S4).

Summarizing, we introduce a precise and efficient CLEM preparation method, which (1) circumvents the need of artificial fiducials, (2) is compatible with widely accessible optical microscopic techniques, and (3) is suitable for various scientific questions.

METHODS

All methods can be found in the accompanying Transparent Methods supplemental file.

	Pro	Con
"Flat embedding"	Fast Cheap Nondisruptive Suitable for all kind of tissues	Limited in vibratome section thickness of 50 μm
NIRB (Bishop et al., 2011)	Fast Suitable for all kind of tissues	Disruptive Fs-laser needed
DAB (Sonomura et al., 2013)	Direct visualization of the target structure	Masking ultrastructure
QDs (Masich et al., 2006)	Suitable for all kind of tissues	Masking ultrastructure Limited tissue penetration

Table 1. Comparison of Common CLEM Protocols
NIRB, near-infrared branding; DAB, diaminobenzidine; QDs, quantum dots

SUPPLEMENTAL INFORMATION

Supplemental Information includes Transparent Methods, four figures, and three videos and can be found with this article online at https://doi.org/10.1016/j.isci.2018.07.012.

AUTHOR CONTRIBUTIONS

J.H. and G.W. designed and led all aspects of the project. M.L., S.B., and S.F. performed most of the experiments. M.L., S.B., S.F., and M.S. analyzed the data. J.H., S.B., and S.F. interpreted data; M.L. and G.W. performed FIB/SEM; S.B., S.F., Y.N., and E.H. performed LM; M.L., M.S., and S.B. reconstructed FIB-SEM datasets; and M.L., S.B., S.F., and G.W. wrote the paper. All authors edited the paper.

DECLARATIONS OF INTERESTS

The authors declare no competing interests.

REFERENCES

Araque, A., Parpura, V., Sanzgiri, R.P., and Haydon, P.G. (1999). Tripartite synapses: glia, the unacknowledged partner. Trends Neurosci. 22, 208–215.

Belu, A., Schnitker, J., Bertazzo, S., Neumann, E., Mayer, D., Offenhäusser, A., and Santoro, F. (2016). Ultra-thin resin embedding method for scanning electron microscopy of individual cells on high and low aspect ratio 3D nanostructures. J. Microsc. 263, 78–86.

Bernardinelli, Y., Nikonenko, I., and Muller, D. (2014). Structural plasticity: mechanisms and contribution to developmental psychiatric disorders. Front. Neuroanat. https://doi.org/10.3389/fnana.2014.00123.

Bishop, D., Nikić, I., Brinkoetter, M., Knecht, S., Potz, S., Kerschensteiner, M., and Misgeld, T. (2011). Near-infrared branding efficiently correlates light and electron microscopy. Nat. Methods 8, 568–570.

Blazquez-Llorca, L., Hummel, E., Zimmerman, H., Zou, C., Burgold, S., Rietdorf, J., and Herms, J. (2015). Correlation of two-photon in vivo imaging and FIB/SEM microscopy. J. Microsc. 259, 129–136.

Bourne, J.N., and Harris, K.M. (2008). Balancing structure and function at hippocampal dendritic spines. Annu. Rev. Neurosci. 31, 47–67.

de Boer, P., Hoogenboom, J.P., and Giepmans, B.N.G. (2015). Correlated light and electron microscopy: ultrastructure lights up! Nat. Methods 12, 503–513.

Feng, G., Mellor, R.H., Bernstein, M., Keller-Peck, C., Nguyen, Q.T., Wallace, M., Nerbonne, J.M., Lichtman, J.W., and Sanes, J.R. (2000). Imaging neuronal subsets in transgenic mice expressing multiple spectral variants of GFP. Neuron 28, 41–51.

Genoud, C., Quairiaux, C., Steiner, P., Hirling, H., Welker, E., and Knott, G.W. (2006). Plasticity of astrocytic coverage and glutamate transporter expression in adult mouse cortex. PLoS Biol. 4, e343.

Grabenbauer, M. (2012). Correlative light and electron microscopy of GFP. Methods Cell Biol. 111, 117–138.

Grabenbauer, M., Geerts, W.J.C., Fernadez-Rodriguez, J., Hoenger, A., Koster, A.J., and Nilsson, T. (2005). Correlative microscopy and electron tomography of GFP through photooxidation. Nat. Methods 2, 857–862.

Heller, J.P., and Rusakov, D.A. (2015). Morphological plasticity of astroglia: understanding synaptic microenvironment. Glia *63*, 2133–2151.

Jung, C.K.E., and Herms, J. (2014). Structural dynamics of dendritic spines are influenced by an environmental enrichment: an in vivo imaging study. Cereb. Cortex *24*, 377–384.

Karreman, M.A., Hyenne, V., Schwab, Y., and Goetz, J.G. (2016a). Intravital correlative microscopy: imaging life at the nanoscale. Trends Cell Biol. *26*, 848–863.

Karreman, M.A., Mercier, L., Schieber, N.L., Solecki, G., Allio, G., Winkler, F., Ruthensteiner, B., Goetz, J.G., and Schwab, Y. (2016b). Fast and precise targeting of single tumor cells in vivo by multimodal correlative microscopy. J. Cell Sci. *129*, 444–456.

Karreman, M.A., Mercier, L., Schieber, N.L., Shibue, T., Schwab, Y., and Goetz, J.G. (2014). Correlating intravital multi-photon microscopy to 3D electron microscopy of invading tumor cells using anatomical reference points. PLoS One *9*, e114448.

Kizilyaprak, C., Bittermann, A.G., Daraspe, J., and Humbel, B.M. (2014). FIB-SEM tomography in biology. Methods Mol. Biol. *1117*, 541–558.

Knott, G.W., Holtmaat, A., Trachtenberg, J.T., Svoboda, K., and Welker, E. (2009). A protocol for preparing GFP-labeled neurons previously imaged in vivo and in slice preparations for light and electron microscopic analysis. Nat. Protoc. *4*, 1145–1156.

Kolotuev, I., Bumbarger, D.J., Labouesse, M., and Schwab, Y. (2012). Targeted ultramicrotomy: a valuable tool for correlated light and electron microscopy of small model organisms. Methods Cell Biol. *111*, 203–222.

Kukulski, W., Schorb, M., Welsch, S., Picco, A., Kaksonen, M., and Briggs, J.A.G. (2012). Precise, correlated fluorescence microscopy and electron tomography of lowicryl sections using fluorescent fiducial markers. In Methods in Cell Biology, T. Müller-Reichert and P. Verkade, eds. (Elsevier), pp. 235–257.

Li, J., Erisir, A., and Cline, H. (2011). In vivo time-lapse imaging and serial section electron microscopy reveal developmental synaptic rearrangements. Neuron *69*, 273–286.

Lucas, M.S., Günthert, M., Bittermann, A.G., de Marco, A., and Wepf, R. (2017). Correlation of live-cell imaging with volume scanning electron microscopy. Methods Cell Biol. *140*, 123–148.

Luckner, M., and Wanner, G. (2018). Precise and economic FIB/SEM for CLEM: with 2 nm voxels through mitosis. Histochem. Cell Biol. 1–22.

Maco, B., Holtmaat, A., Cantoni, M., Kreshuk, A., Straehle, C.N., Hamprecht, F.A., and Knott, G.W. (2013). Correlative in vivo 2 photon and focused ion beam scanning electron microscopy of cortical neurons. PLoS One *8*, e57405.

Maco, B., Holtmaat, A., Jorstad, A., Fua, P., and Knott, G.W. (2014). Correlative in vivo 2-photon imaging and focused ion beam scanning electron microscopy. In Methods in Cell Biology, T. Müller-Reichert and P. Verkade, eds. (Elsevier), pp. 339–361.

Masich, S., Östberg, T., Norlén, L., Shupliakov, O., and Daneholt, B. (2006). A procedure to deposit fiducial markers on vitreous cryo-sections for cellular tomography. J. Struct. Biol. *156*, 461–468.

Mironov, A.A., and Beznoussenko, G.V. (2009). Correlative microscopy: a potent tool for the study of rare or unique cellular and tissue events. J. Microsc. *235*, 308–321.

Ostroff, L.E., Manzur, M.K., Cain, C.K., and LeDoux, J.E. (2014). Synapses lacking astrocyte appear in the amygdala during consolidation of Pavlovian threat conditioning. J. Comp. Neurol. *522*, 2152–2163.

Panatier, A., Arizono, M., and Nagerl, U.V. (2014). Dissecting tripartite synapses with STED microscopy. Philos. Trans. R. Soc. Lond. B Biol. Sci. *369*, 20130597.

Schain, A.J., Hill, R.A., and Grutzendler, J. (2014). Label-free in vivo imaging of myelinated axons in health and disease with spectral confocal reflectance microscopy. Nat. Med. *20*, 443–449.

Schieber, N.L., Machado, P., Markert, S.M., Stigloher, C., Schwab, Y., and Steyer, A.M. (2017). Minimal resin embedding of multicellular specimens for targeted FIB-SEM imaging. Methods Cell Biol. *140*, 69–83.

Sonomura, T., Furuta, T., Nakatani, I., Yamamoto, Y., Unzai, T., Matsuda, W., Iwai, H., Yamanaka, A., Uemura, M., and Kaneko, T. (2013). Correlative analysis of immunoreactivity in confocal laser-scanning microscopy and scanning electron microscopy with focused ion beam milling. Front. Neural Circuits *7*, 26.

Witcher, M.R., Kirov, S.A., and Harris, K.M. (2007). Plasticity of perisynaptic astroglia during synaptogenesis in the mature rat hippocampus. Glia *55*, 13–23.

Supplemental Information

Label-free 3D-CLEM

Using Endogenous Tissue Landmarks

Manja Luckner, Steffen Burgold, Severin Filser, Maximilian Scheungrab, Yilmaz Niyaz, Eric Hummel, Gerhard Wanner, and Jochen Herms
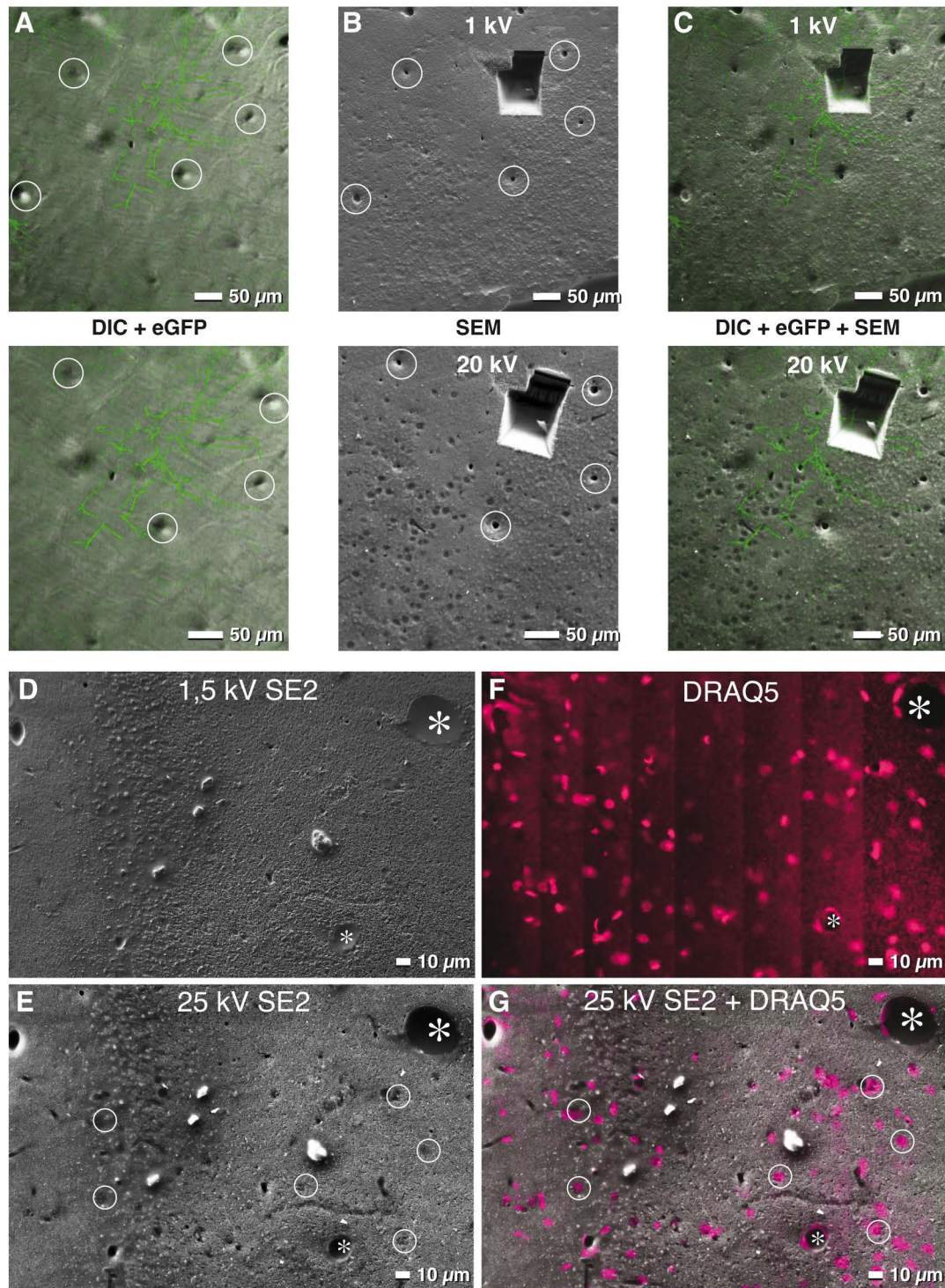
Figure S1. Vibratome sections at different kV, Related to Figure 1

(A) DIC images taken from the surface of the vibratome section and merged with a projection view of the dendrites (green = eGFP).

(B) SEM micrographs at different kV. Topographic and material contrast change are enhanced with increase of the accelerating voltage: Blood vessels are easily recognized as little holes (circles) at low and high kV. Sectioned nuclei with almost no topographic contrast at 1 kV, show a strong material contrast at 20 kV.

(C) Superimpostion of a DIC stack and an eGFP stack allows a precise localization of the target dendrite(s) in a range of a few μm.

(D-E) SEM micrographs at different kV. Different high voltages can be chosen to enhance either the topographic or material contrast of nuclei (circles): 1,5 kV (D) and 25 kV (E).

(F) From the DRAQ5 stack, 7 segments of different height in the stack were combined into a stitched image, representing only surface near nuclei.

(G) Superposition of micrographs enables precise correlation of nuclei (circles) and blood vessels (asterisk) in both, SEM an LSM.
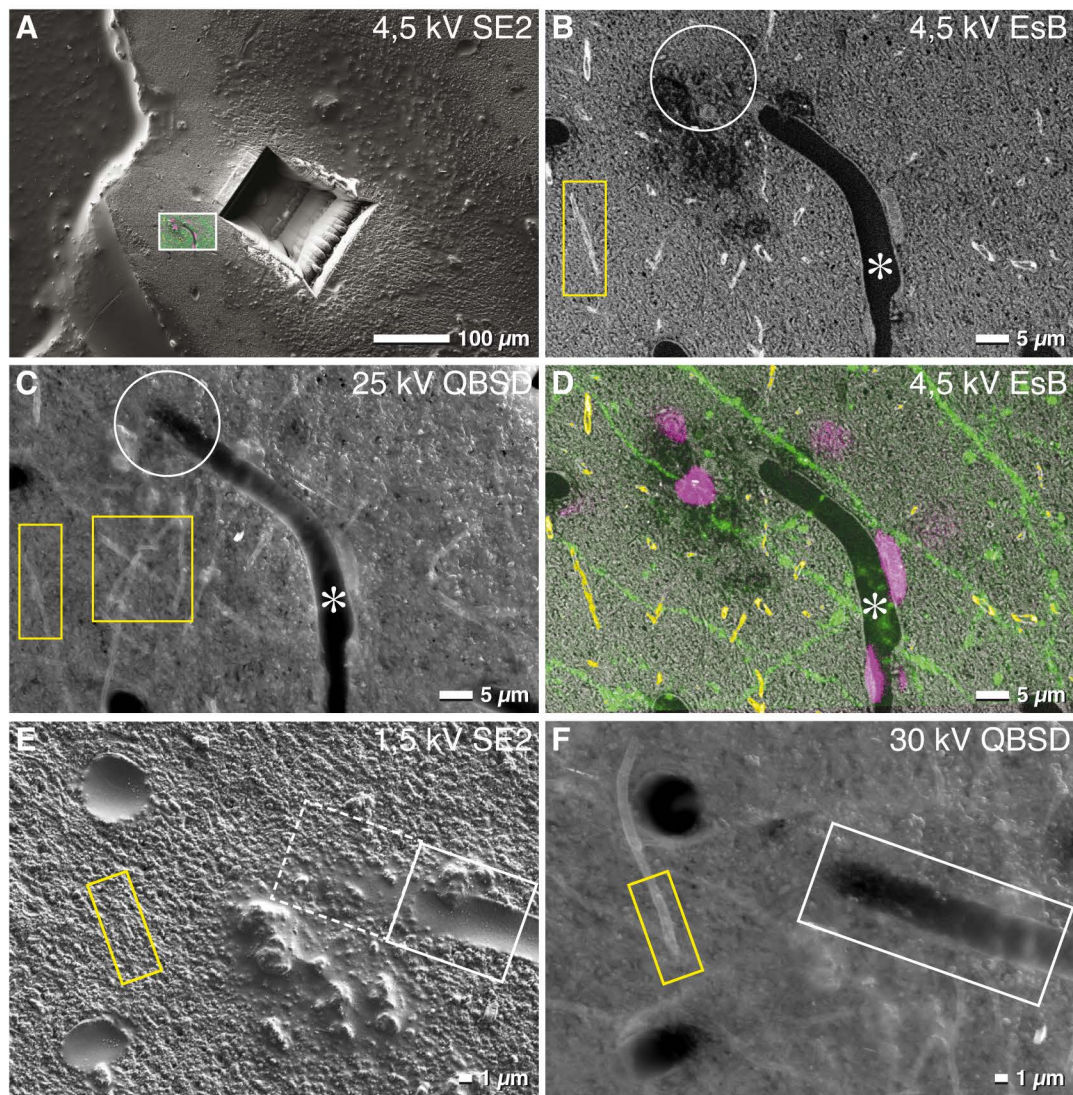
Figure S2. Myelinated axons in SEM, Related to Figure 1 and 2

(A) SEM micrograph of a vibratome slice. The trench indicates a FIB/SEM recorded target volume. Correlation with LM micrograph exhibits the next traget area.

(B-C) Myelinated axons are clearly visible in both, the EsB image at moderate kV (B) or in the QBSD image at high kV (C) due to their strong staining with osmium.

(D) Overlay of myelinated axons (yellow), nuclei (magenta) and dendrites (green) confirm the precision of surface correlation of CLSM and SEM. Blood vessels display at higher voltages a dark contrast (asterisk) or are visible at low kV by topographic contrast of the SE2 image (A).

(E-F) Comparison of 1,5 kV SE2 image (framed areas) with the QBSD image demonstrates the depth information given at high kV. Myelinated axons are clearly visible at high kV (F = yellow frame) and undetectable in the SE2-image (E = yellow frame).
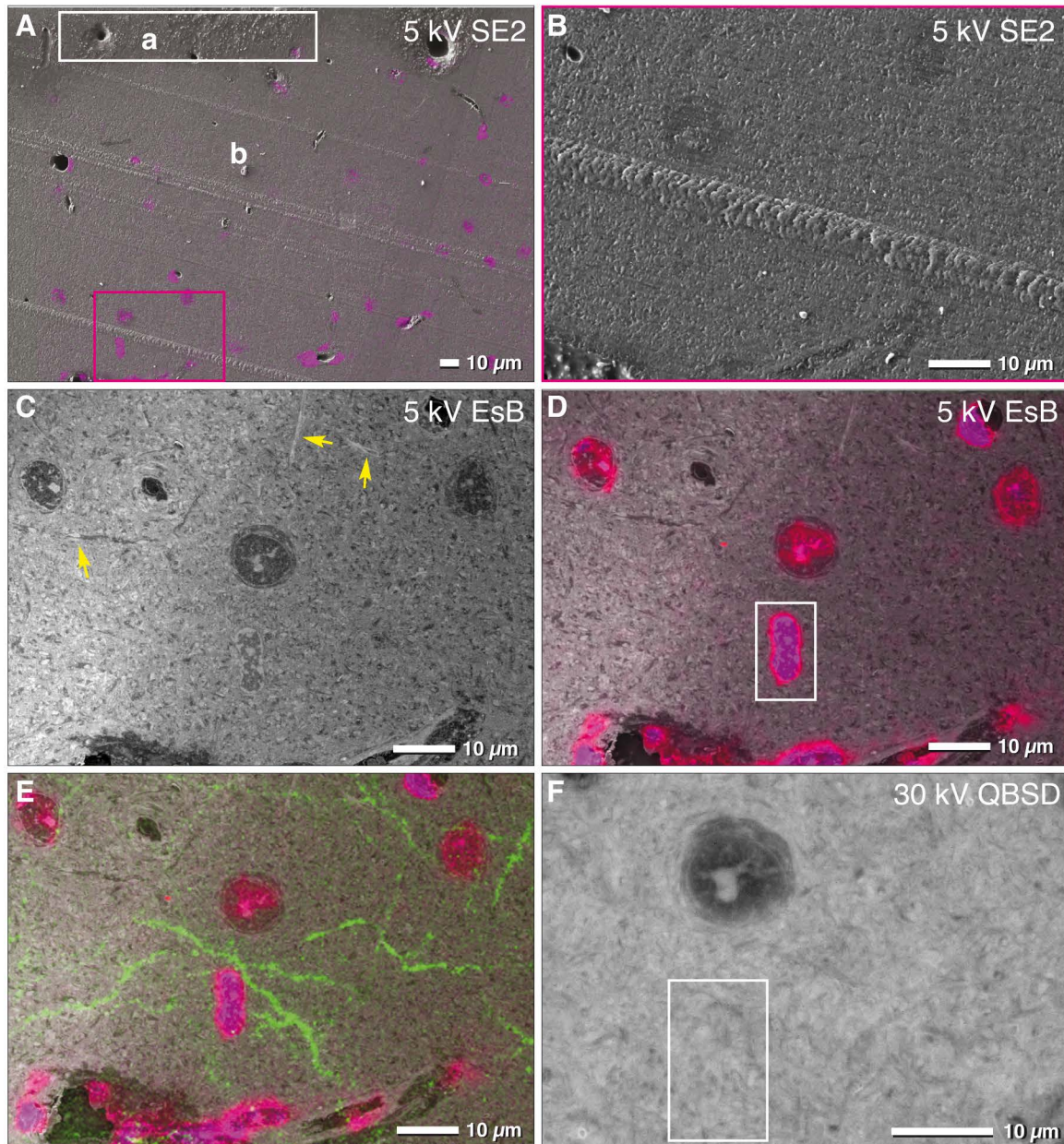
Figure S3. Enhancement of the material contrast after smoothing of vibratome sections, Related to Figure 1 and 2

(A) Correlation of light micrographs of stained nuclei (DRAQ5; LSM) with SEM micrographs of an embedded mouse brain section. For high resolution correlation, the specimen surface was smoothed by removal of few µm with a glass knife equipped ultra microtome. The difference in surface topography can be compared before (a = framed area; white) and after smoothing (b).

(B-E) At high magnification (framed area of A; magenta) nuclear details (nuclear envelope, heterochromatine) can be hardly recognized in the SE2 image (B) but they are clearly visible with the EsB-signal (C and D 5; kV). Axons (arrows) can be identified by their myelin sheets which give a high contrast due to the strong osmium staining. Superposition with the LM image of the nuclei (magenta) and dendrites (green) enable a precise correlation in the sub-micrometer range (E).

(F) The depth information is increased with high accelerating voltage (30 kV). Contrast of tangential sectioned nuclei becomes reduced (framed area; compare with framed area in D).
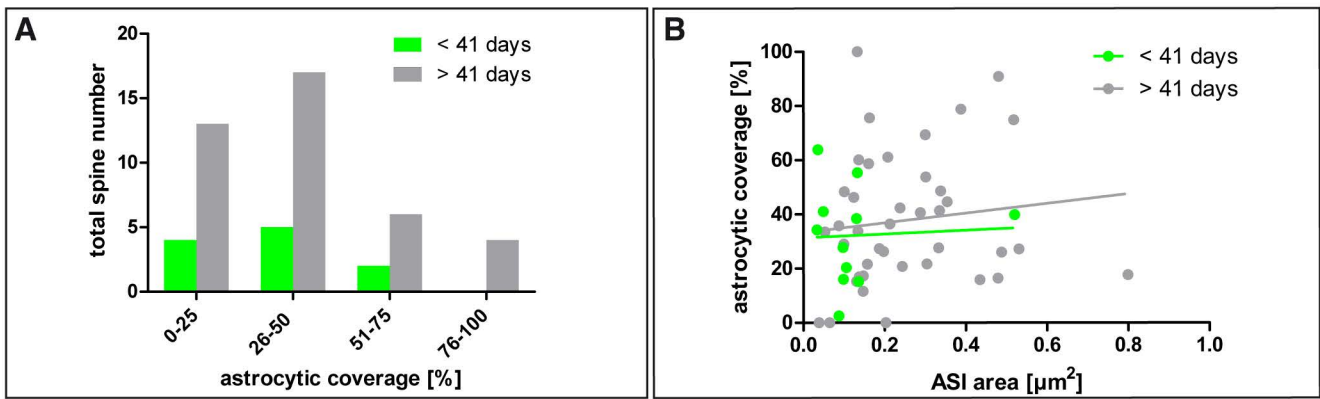
Figure S4. Astrocytes equally cover the synaptic perimeter of young and old spines, Related to Figure 4

(A) Distribution graphs of young (≤ 41 days) and old (≥ 41 days) dendritic spines according to astrocytic coverage of the synaptic perimeter.

(B) Correlation between astrocytic coverage and ASI area of young (≤ 41 days) and old (≥ 41 days) dendritic spines.

Transparent Methods

Animals

Female and male 2-3 months old heterozygous GFP-M mice (Tg(Thy1-EGFP)MJrs from Jackson Laboratory, Bar Harbor, Maine) were used (Feng et al., 2000). Mice were group-housed under pathogen-free conditions and bred in the animal housing facility of the Center of Stroke and Dementia Research, with food and water provided ad libitum (21 ± 1°C, at 12/12 hour light/dark cycle). All experiments were carried out in compliance with the National Guidelines for Animal Protection, Germany with the approval of the regional Animal care committee of the Government of Upper Bavaria, and were overseen by a veterinarian.

Cranial window implantation

Before use, surgical tools were sterilized in a glass-bead sterilizer (FST). Mice were anesthetized by an intra-peritoneal injection of ketamine/xylazine (140/10 mg/kg body weight, WDT, Bayer Health Care). In order to prevent cerebral edema Dexamethasone (6 mg/kg body weight, Sigma Aldrich) was injected intraperitoneally. Subsequently, mice were placed onto a heating blanket (37 °C) and the head was fixed in a stereotactic frame. Eyes were protected from drying by applying eye-ointment (Bepanthen, Bayer). The scalp was washed with swabs soaked with 70 % ethanol. A flap of skin covering the cranium was excised using small scissors. The periosteum was scraped away with a scalpel. The prospective craniotomy location (1.5-2.5 mm AP and 0-4 mm ML relative to bregma) was marked with a biopsy punch (diameter 4 mm, Integra LifeSciences). The exposed skull around the area of interest was covered with a thin layer of dental acrylic (iBond Self Etch, Hereaus Kulzer) and hardened with a LED polymerization lamp (Demi Plus, Kerr). A dental drill (Schick Technikmaster C1, Pluradent) was used to thin the skull around the marked area. After applying a drop of sterile phosphate buffered saline (DPBS, Gibco, Life Technologies) on the craniotomy the detached circular bone flap was removed with forceps. A circular coverslip (4 mm diameter, VWR International) was placed onto the craniotomy and glued to the skull with histoacryl adhesive (Aesculap). The exposed skull was covered with dental acrylic (Tetric Evoflow A1 Fill, Ivoclar Vivadent) and a head-post was attached parallel to the window for head-fixing mice in subsequent imaging sessions. After surgery, mice received a subcutaneous dose of the analgesic Carprophen (7.5 mg/kg body weight, Rimadyl, Pfizer) and antibiotic Cefotaxim (5

mg/kg body weight, Pharmore). Finally, mice were allowed to recover from surgery on a heating blanket.

Chronic *in vivo* two-photon microscopy

In vivo two-photon imaging started 4 weeks after cranial window implantation, using a multiphoton LSM 7 MP microscope (Zeiss) equipped with a fs-laser (Mai Tai DeepSee, Spectra-Physics), a 20x water immersion objective (W Plan-Apochromat 20x/1.0 NA, Zeiss) and a motorized stage. eGFP was excited at 920 nm and the emission was collected after a band pass filter from 470-550 nm by a non-descanned detector (photomultiplier tube GaAsP, Zeiss) directly after the objective. Throughout the imaging sessions, mice were anesthetized with isoflurane (1 % in oxygen, 0.5 l/min) and placed on a heating pad to keep body temperature at 37 °C (Fine Science Tools GmbH). A magnified image of the superficial cerebral blood vessels was acquired by using the camera port of the 7 MP microscope. The same ROIs were repositioned over time by alignment of the field of view based on the vascular pattern. Apical dendritic tufts of layer V pyramidal neurons in the somatosensory cortex were imaged in consecutive sessions at specified time points. For overview images, 3D stacks of 300 μm depth with 3 μm axial resolution and 1024×1024 pixels per image frame (0.4 μm/pixel) were acquired in multiphoton mode of the microscope. To resolve dendritic spines, high-resolution images from single dendrites were taken with 1 μm axial resolution and 512 × 256 pixels per image frame (0.1 μm per pixel). Individual imaging sessions lasted for no longer than 60 min with the laser power kept below 50 mW to avoid phototoxicity. Special care was taken to ensure consistent fluorescence levels both in space and time. After the fourth imaging session mice were placed into an enriched environment accordingly to a recently published protocol to enhance the structural plasticity of dendritic spines (Jung and Herms, 2014).

Preparation of brain sections

Mice were transcardially perfused with a mixture of formaldehyde and glutardialdehyde (Electron Microscopy Sciences, EMS) in PBS. A mixture of 0.5 % glutardialdehyde and 3.5 % formaldehyde was used in order to reduce background fluorescence from glutardialdehyde while preserving eGFP fluorescence and specimen ultrastructure. After 1 h perfusion mice were decapitated and the right

parietal bone with the ipsilateral window was removed. Subsequently, the mouse head was attached via head post to the stage of a vibratome (VT1000S, Leica Biosystems) to cut the brain tissue parallel to the imaging plane. This way, a single brain slice containing all cortical layers and the complete somato-sensory cortex was obtained. The cortical brain slice was incubated in 4% formaldehyde in PBS overnight at 4 °C, washed with PBS at the next day and subsequently stored in PBS at 4 °C. The fixed brain slice was further cut into 50 µm sections on a vibratome. Care was taken to keep the order of all obtained slices from top to bottom as well as not to flip them. Each slice was mounted onto a Cell-Tak™ (Corning®, Thermo Fisher Scientific) coated microscope slide (Superfrost, Menzel) with an adhesive, circular imaging spacer (Secure-Seal™, Grace Bio-Labs). The well of the imaging spacer was filled with 20 µM DRAQ5 (Biostatus) solution, sealed with a coverslip (No. 1.5, Zeiss) and incubated overnight at 4 °C.

LM microscopy

Slides were imaged in "tile scan" mode of an Apotome.2 wide field microscope (Zeiss) equipped with an EC Plan-NEOFLUAR 10x / 0.3 NA objective (Zeiss) to identify brain slices with the desired regions of interest. For bright field microscopy, the illumination aperture (NA 0.1) of the condenser was closed to increase image contrast. Emission of eGFP and DRAQ5 was collected using standard filter sets for green (490-606 nm) and far red (643-752 nm) (Zeiss). Confocal imaging was used (LSM 880 with AiryScan, Zeiss) to map all natural landmarks in 3D. Overview images of the region of interest with 3 µm axial resolution and 1024 × 1024 pixels per image frame (0.4 µm/pixel) were acquired with a Plan-Apochromat 20x / 0.8 NA air objective. High resolution image stacks (135 x 135 x 50 μm^3 with 0.13 µm in xy and 1 µm in z per pixel) of dendrites were acquired with a Plan-Apochromat 63x / 1.4 oil objective (Zeiss). DRAQ5 and eGFP were excited at 633 nm and 488 nm, respectively. Emission was collected from 500-560 nm (eGFP) and 650-700 nm (DRAQ5). Additionally, differential interference contrast images were acquired in the transmitted light channel. Furthermore, spectral confocal reflectance microscopy was used to visualize myelinated axons within the same volume. Axons were imaged with laser lines of 458 nm, 514 nm and 633 nm in a single track. The reflection mode of the microscope was used in combination with a partial mirror (80 % transmission, 20

% reflection) as main beam splitter. Images of all three channels were combined by using the average function of the Zen software (Version 2.3, Zeiss).

EM preparation

After light microscopic inspection mounted vibratome sections were uncovered by removal of the coverslip. Subsequently, samples were washed with cacodylate buffer (75 mM cacodylate 75 mM NaCl, 2 mM $MgCl_2$) and again fixed with 2,5 % glutardialdehyde in cacodylate buffer for 15 min, followed by 3 washing steps in cacodylate buffer. The tissue was post-fixed with 1 % OsO_4 and 1 % $K_4Fe(CN)_6$ in cacodylate buffer for 30 min, washed 3 times in ddH_2O, incubated with 1 % thiocarbohydrazide in ddH_2O for 30 minutes, washed with ddH_2O 3 times, followed by a second post-fixation with 1 % OsO_4 in ddH_2O for 30 min. Samples were further rinsed 3 times with ddH_2O, dehydrated in a graded series of acetone and incubated in 1 % uranyl acetate with 20 % acetone for 30 min. Subsequently, sections were embedded on the glass slide and infiltrated with 1:1 Hard-Plus Resin-812 in acetone for 10 minutes, 2:1 Hard-Plus Resin-812 in acetone for 30 min and finally in 100 % Hard-Plus Resin-812 for 1h at RT. Excessive resin was removed by centrifugation: the slide was placed in a 50 ml falcon tube with a tissue paper at the bottom and centrifuged at 1000 rpm for 2 min. After samples were polymerized for 3 days at 60 °C, the glass was trimmed with a diamond pen and mounted on an aluminum stub with colloidal silver. Finally, the glass was covered with colloidal silver and the entire sample was carbon coated (thickness of 15-20 nm) by evaporation.

FIB/SEM microscopy

Mouse brain tissues were imaged in an Auriga 40 FIB/SEM workstation (Carl Zeiss Microscopy GmbH) operating under SmartSEM (Carl Zeiss Microscopy GmbH) and Atlas3D software (Fibics Inc., Ottawa, Ontario, Canada). To facilitate correlation, the 50 µm thick brain slice was milled down to the surface of the glass slide, which was used as a reference. Subsequently, a 70 µm long ramp was milled by FIB (for vibratome sections with a thickness of 50 µm and a FIB tilt angle of 54°, the length of the milling ramp can be calculated as tan54° = 1.374. In this case, the trapezoid trench has to be approx. 70 µm long). After milling of 20 µm in z-direction milling was stopped, the ion beam current reduced to 10 nA, and the milling depth increased to

10-20 µm. After additional 20 µm of length, the trench was milled with a depth of 30 µm, until the beam reaches the glass slide. While milling the ramp to get access to the target volume, key frames were taken to inspect the correlation landmarks (blood vessels, nuclei and myelinated axons) to determine the position of the target dendrite in all three dimensions. Final milling parameters were set to 1-2 nA milling current of the Ga-emitter. With each cycle 10-15 nm of epoxy resin was removed. SEM images were recorded with an aperture of 60 µm in the high current mode at 1.5 kV of the in-lens EsB detector with the EsB grid set to -800-1200 V. Key frames were imaged with a pixel size of 20-27 nm and the ROI with a pixel size of 5-8 nm. Images series of 3000-4000 sections were recorded. In the synchronous mode of the ATLAS-System, the milling current and depth were adjusted to match milling time with exposure time set to 1 min. Automatic correction of focus (*auto tune*) and astigmatism (*auto stig*) was applied every 30 minutes.

3D reconstruction of LM and FIB/SEM image stacks

LM images of blood vessels, nuclei and myelinated axons were reconstructed in 3D using Imaris (Version 7.7.2, Bitplane). FIB/SEM image stacks were aligned, segmented and 3D reconstructed in Amira (FEI Company). For registration of the LM and FIB/SEM datasets, both 3D reconstructions were fit into each other manually by rotation and translation. FIB/SEM volume was used as a reference to adjust the LM/DIC reconstruction. Registration was performed by successive alignation of blood vessels, nuclei and finally myelinated axons to increase the precision of the correlation.

Image analysis

Amira 3D reconstructions of dendritic spines, corresponding presynapses and perisynaptic astrocytic processes were imported in Blender software for morphometric analysis. Volumes, surfaces and axon spine interfaces (ASI) were quantified with the plugins "NeuroMorph Measurement Tools" and "NeuroMorph Proximity Analysis" (Jorstad, A., Nigro, B., Cali, C. *et al.* 2015 and Barnes *et al.* 2015). Astrocytic coverage was quantified by measuring the total perimeter of the ASI and the proportion that was covered by the astrocyte. To calculate distance distributions of endogenous landmarks in GraphPad Prism 5, distances between 10 randomly chosen dendrites and their closest natural landmarks were measured and

quantified with the 3D measurement tool in Imaris (Version 7.7.2, Bitplane). Dendritic spine lifetime was determined manually off-line by analyzing the corresponding 2-photon micrograph time series. Dendritic spines were defined as stable if their locations did not change along the dendritic shaft between consecutive imaging sessions (acceptable range < 1 µm). Spines, which emerged or disappeared over two consecutive imaging sessions, were assigned as newly gained or lost, respectively. Resolution limitations in the z-plane restricted our analysis to laterally protruding spines. For illustration purpose only, image stacks were deconvolved (AutoQuantX2, Media Cybernetics) and adjusted for contrast and brightness. Figures were created in Adobe Photoshop/Illustrator CS6 and supplementary movies were made in Amira (Thermo Fisher Scientific™).

Key Resource Table

REAGENT or RESOURCE	SOURCE	IDENTIFIER
Chemicals, Peptides, and Recombinant Proteins		
20% Formaldehyde	SCIENCE SERVICES	Cat# E15713
25% Glutardialdehyde	SCIENCE SERVICES	Cat# E16216
Cell-Tak™	Thermo Fisher Scientific	Cat# 10317081
DAPI	Thermo Fisher Scientific	Cat# D1306
DRAQ5	Biostatus	Cat# DR50050
Fetal Bovine Serum (FBS)	GIBCO	Cat# 10270-106
Osmium Tetroxide	SCIENCE SERVICES	Cat# E19130
PBS	GIBCO	Cat# 20012-068
Potassium hexacyanoferrate(II) trihydrate	Sigma-Aldrich	Cat# 455946
Sodium cacodylate trihydrate	MERCK	Cat# 20840-100G-F
Thiocarbohydrazide	Sigma-Aldrich	Cat# 223220
Experimental Models: Organisms/Strains		
Mouse: STOCK Tg(Thy1-EGFP)MJrs/J	The Jackson Laboratory	Stock# 007788
Software and Algorithms		
Adobe Photoshop CC	Adobe Systems Software Ireland Limited	http://www.adobe.com
Altlas3D	Fibics Inc.	
Amira 6.2	Thermo Fisher Scientific	https://www.fei.com/software/amira-3d-for-life-sciences/

Blender Plugin: NeuroMorph Measurement Tools NeuroMorph Proximity Analysis	The Blender Foundation	https://www.blender.org/
GraphPad Prism	GraphPad Software Inc,	http://www.graphpad.com/scientific-software/prism/
ImageJ (1.50, Java 1.8.0_60, 64 bit)	NIH	https://imagej.nih.gov/ij/; RRID:SCR_003070
Imaris 7.7.2	Bitplane	http://www.bitplane.com/
SmartSEM	Carl Zeiss Microscopy GmbH	N/A
Zen 2.3	Carl Zeiss Microscopy GmbH	N/A